

**Environmental controls on simulated deep moist convection initiation
occurring during RELAMPAGO-CACTI**

T. Connor Nelson,^{a, b} James Marquis,^{c, b} John M. Peters,^d and Katja Friedrich,^b

^a *Cooperative Institute for Research in the Atmosphere and NOAA/NWS Operations Proving
Ground, Kansas City, Missouri*

^b *Department of Atmospheric and Oceanic Sciences, University of Colorado Boulder, Boulder,
Colorado*

^c *Pacific Northwest National Laboratory, Richland, Washington*

^d *Department of Meteorology, U.S. Naval Postgraduate School, Monterey, California*

Corresponding author: T. Connor Nelson, tconnorn@colostate.edu

11 ABSTRACT: This study synthesizes the results of 13 large eddy simulations of deep convective
12 updrafts forming over idealized terrain using environments observed during the RELAMPAGO and
13 CACTI field projects. Using composite soundings from multiple observed cases, and variations
14 upon them, we explore the sensitivity of updraft properties (e.g., size, buoyancy, and vertical pres-
15 sure gradient forces) to influences of environmental relative humidity, wind shear, and mesoscale
16 orographic forcing that support or suppress deep convection initiation (CI). Emphasis is placed on
17 differentiating physical processes affecting the development of updrafts (e.g., entrainment-driven
18 dilution of updrafts) in environments typifying observed successful and null (i.e., no CI despite
19 affirmative model forecasts) CI events.

20 Thermally-induced mesoscale orographic lift favors the production of deep updrafts originating
21 from ~ 1 – 2 -km-wide boundary layer thermals. Simulations without terrain forcing required much
22 larger (~ 5 -km-wide) thermals to yield precipitating convection. CI outcome was quite sensitive to
23 environmental relative humidity; updrafts with increased buoyancy, depth, and intensity thrived in
24 otherwise inhospitable environments by simply increasing the free tropospheric relative humidity.
25 This implicates the entrainment of free-tropospheric air into updrafts as a prominent governor of
26 CI, consistent with previous studies. Sensitivity of CI to the environmental wind is manifested by:
27 1) low-level flow affecting the strength and depth of mesoscale convergence along the terrain, and 2)
28 clouds interacting with vertical wind shear in the free-troposphere encounter updraft-suppressing
29 pressure gradient forces. Among the ensemble of thermals occurring in each simulation, the widest
30 deep updrafts in each simulation were the most sensitive to environmental influences.

31 1. Introduction

32 Deep moist convection initiation (CI) is a challenging process to represent in numerical weather
33 prediction and climate models, and presents a notoriously difficult weather forecasting problem.
34 Forecast uncertainties stem from the dependency of CI on complex processes that interact across
35 a wide range of $O[10^{-1}-10^2 \text{ km}]$ scales (Xue and Martin 2006; Duda and Gallus 2013; Moser and
36 Lasher-Trapp 2017). Due to this wide range of scales, operational mesoscale numerical weather
37 prediction must rely on a mix of cumulus, turbulence, microphysics, and convective boundary layer
38 parameterization schemes to represent much of the CI process acting on subgrid scales (e.g., Davis
39 et al. 2003; Trier et al. 2004, 2011; Wilson and Roberts 2006; Weisman et al. 2008; Duda and
40 Gallus 2013; Rousseau-Rizzi et al. 2017).

41 Many recent studies of large eddy simulation (LES) show that processes critical to CI are
42 under-resolved by typical operational mesoscale forecast models. For example, cumulus and
43 cumulonimbus clouds are composed of discrete, positively buoyant thermals that interact with the
44 environment through entrainment that occurs on scales that are typically smaller than the lower
45 resolution limit of mesoscale models (French et al. 1999; Damiani et al. 2006; Houston and Niyogi
46 2007; Varble et al. 2014; Moser and Lasher-Trapp 2017; Rousseau-Rizzi et al. 2017; Morrison
47 2017; Hernandez-Deckers and Sherwood 2016, 2018; Peters et al. 2020). CI is strongly influenced
48 by the entrainment-driven dilution of core updraft buoyancy (Zhao and Austin 2005; Romps 2010;
49 De Rooy et al. 2013; Morrison 2017; Hernandez-Deckers and Sherwood 2016, 2018; Morrison
50 et al. 2020; Peters et al. 2020). All other conditions being equal, the rate at which buoyancy is
51 diluted is inversely proportional to the width of the buoyant thermal (Morrison 2017; Lecoanet and
52 Jeevanjee 2019; Morrison et al. 2020; Peters et al. 2020). Thus, entrainment will tend to inhibit CI
53 associated with narrower clouds to a greater extent than with wider clouds. Morrison et al. (2021)
54 and Peters et al. (2021a,b) argue that the width of the region of sub-cloud ascent that triggers a
55 cloud, and ultimately influences a cloud's width, is a critical factor in determining whether or not
56 CI will occur.

57 Orography often promotes CI through the production of sub-cloud updrafts via solar heating of
58 elevated terrain and 'mechanically-forced' updrafts by the mesoscale flow impinging on it (e.g.,
59 Kirshbaum et al. 2018). These factors are likely to modulate the size of updrafts within the planetary
60 boundary layer, and by extension, the likelihood of CI (Marquis et al. 2021). Other environmental

61 factors influencing CI include relative humidity (RH) and vertical shear of the horizontal wind in
62 the “free troposphere” (i.e., the layer of the troposphere located above the boundary layer). Recent
63 modeling studies show that the effects of entrainment are more detrimental when free-tropospheric
64 RH is relatively small (Morrison 2016; Morrison et al. 2020, 2021; Peters et al. 2020). Together,
65 RH and the width of the sub-cloud updraft determine whether or not CI occurred in the idealized
66 simulations of Morrison et al. (2021). Some studies have implied that shear may directly modify
67 turbulent entrainment processes (e.g., Wang et al. 2008, 2012), while others implicate downward-
68 pointing vertical pressure gradient forces resulting from shear-updraft dynamic interactions that
69 decelerate ascending thermals and stifle deepening clouds (Peters et al. 2019). However, the
70 relative roles of RH, wind shear effects, and terrain-flow interactions play on cloud-scale updrafts
71 in observed environments is not well understood.

72 The Remote Sensing of Electrification, Lightning, and Mesoscale/Microscale Processes with
73 Adaptive Ground Observations (RELAMPAGO; Nesbitt et al. 2021) project, and the companion
74 Cloud, Aerosol, and Complex Terrain Interactions (CACTI; Varble et al. 2021) field campaign
75 aimed to better understand the interaction between the mesoscale environment and complex terrain
76 producing CI in central Argentina. These campaigns collected numerous radiosonde soundings
77 within 10–30 km of growing congestus along the Sierras de Córdoba (SDC) range, yielding a
78 large sample of observed near-cloud ambient conditions ideal for testing environmental influences
79 upon CI (Schumacher et al. 2021). In a companion study to this one, Nelson et al. (2021) used
80 the RELAMPAGO-CACTI radiosonde sounding data set to statistically differentiate near-cloud
81 environments associated with a variety of CI outcomes, ranging from environments yielding
82 sustained storms to null events (i.e., no CI despite affirmative forecasts from 3–4 km horizontal
83 resolution convective allowing models). Evaluation of many common operational environmental
84 metrics across cases revealed that null events often contained better convective potential than
85 environments supporting observed CI. However, lower values of free-tropospheric RH in null
86 environments led them to hypothesize that entrainment of free tropospheric air into cloudy updrafts
87 was a prominent factor differentiating CI outcome.

88 In this study, we combined the RELAMPAGO-CACTI sounding data base with storm-scale
89 three-dimensional LES to examine updraft-environment interaction processes governing CI. We
90 specifically address the aforementioned hypothesis regarding the role of free-tropospheric RH

posed by Nelson et al. (2021). We also investigated the influences of vertical wind shear upon cloud-scale CI processes. In doing so, we illustrate the sensitivity of terrain-induced sub-cloud mesoscale ascent to the vertical wind profile and discuss its influence upon the width of deep convective updrafts. The manuscript organization is as follows: section 2 discusses the model configurations and general experimental design, sections 3 and 4 analyze the sensitivity of our results to differing observed and modified environmental conditions, and to model assumptions. The results are discussed in the context of past studies in section 5. Our key findings are summarized in section 6.

2. Methods

We performed 13 high-resolution three-dimensional LESs using the Cloud Model 1 (CM1; Bryan and Fritsch 2002) version 19.8. The CM1 configurations used in this study are summarized in Table 1. The majority of our simulations used a uniform horizontal grid spacing of 250 m and a vertical grid spacing of 125 m over a $270 \times 360 \times 13 \text{ km}^3$ static domain with periodic lateral boundary conditions. Our rationale for the domain vertical extent is that we are focusing on convection relatively early in the life cycle, where it is limited to $\sim 9\text{--}11 \text{ km}$ deep and when complex gravity waves and reflections off of the top of the domain are expected to be minimal. We prescribed a rigid free slip condition at the model top and a Rayleigh damper for altitudes above 10 km with a coefficient of $3.33 \times 10^{-3} \text{ s}^{-1}$ to limit artifacts of waves. Simulations were run with an adaptive timestep (initially 1 s) for 2 hr, and output was saved at 1-min frequency in all but select analyses described in section 3, for which output was saved every 5 s. The surface was semi-slip with a variable surface exchange coefficient for low-wind (Fairall et al. 2003) and high-wind (Donelan et al. 2004) speeds and a constant enthalpy surface exchange coefficient based upon the land-use type. The land-use was specified as grassland (from Weather Research and Forecasting (WRF) model parameterizations) with a soil moisture availability of 0.5 (Nowotarski et al. 2014; Mulholland et al. 2020). Coriolis accelerations were neglected. No boundary layer parameterizations were prescribed. We used the two-moment Morrison microphysics scheme (Morrison et al. 2005).

The majority of our simulations included longwave and shortwave radiation, surface fluxes, and idealized terrain approximating that of the SDC near where the environmental conditions were observed. We prescribed an idealized terrain elevation profile (Z_s ; where s denotes the model

120 surface) consisting of an elliptical-gaussian mountain similar to Mulholland et al. (2020) and
 121 Dörnbrack et al. (2005),

$$Z_s(x, y) = h * [(1 + (\frac{X}{a})^2)^{-1.5}], \quad (1)$$

$$X = \sqrt{(x + \gamma x_{max})^2 + \beta[(\alpha y + \varphi y_{max})^2]}, \quad (2)$$

122 where h is the maximum terrain height¹ (1.25 km), x_{max} and y_{max} are the dimensions of the
 123 model domain in the x- and y-directions (270 km, 360 km, respectively), a is the horizontal half-
 124 width of the ridgeline (15 km), X is a ‘stretching parameter’, γ and φ are factors prescribing the
 125 x- and y-positions of the center of the terrain relative to the model domain center (0.65, 0.10,
 126 respectively), and β and α are stretching coefficients for the entire terrain feature in the north-south
 127 and east-west directions (0.15, 0.40, respectively). We called the WRF-RRTMG radiation scheme
 128 (Iacono et al. 2008) every 15 min, initialized at 16 UTC on 6 November at (-31.97° , -64.68°)
 129 latitude and longitude, which was the mean location and time for the soundings comprising the

¹h was prescribed based on the relative difference of the true peak elevation of the SDC range and the mean height above sea level of the radiosonde launch sites used in this study ($z \sim 1$ km above mean sea level).

TABLE 1. Summary of CM1 specifications and configurations used

Specification	Value
CM1 version	19.8
Model resolution (x, y, z)	0.25x0.25x0.125 km ³
Domain size (x, y, z)	270x360x13 km ³
Grid points (x, y, z)	1080x1440x103
Time step	Adaptive 1-s
Radiation (LW/SW)	WRF-RRTMG (Iacono et al. 2008)
Land use type	WRF-grassland, Soil moisture availability = 0.5
Microphysics	Two-moment Morrison (Morrison et al. 2005)
Terrain	Idealized SDC
Lateral boundary conditions	Periodic
Surface boundary conditions	Semi-slip and Monin-Obukhov (from WRF)
Top boundary conditions	Rigid free slip with Rayleigh damper (> 10 km)
Integration time	2-hr
Subgrid turbulence	TKE; LES
Coriolis acceleration	off
Boundary layer physics	N/A
Cumulus parameterization	none

130 composite soundings. Surface fluxes of heat, moisture, and momentum were parameterized using
131 the summertime WRF-grassland surface model and Monin-Obukhov similarity theory surface
132 model (Grell et al. 1994) following Mulholland et al. (2020). The initial values for the shallow
133 and deep soil temperatures were 299 K and 297 K, which are the default values for CM1. Results
134 from several experiments utilizing this model configuration are analyzed in section 3; while a small
135 subset of sensitivity experiments that exclude terrain, surface fluxes, and radiation are discussed in
136 section 4.

137 Our domain was initialized with horizontally-homogeneous base state variables derived from
138 composite soundings generated by Nelson et al. (2021). Each sounding represents mean near-
139 cloud environments containing: 1) radar-observed initiation of sustained precipitating convection
140 producing near-surface reflectivity > 35 dBZ for at least 20 min (i.e., sustained CI events, hereafter
141 “SCI”; Fig. 1a), 2) radar-detected weak and short-lived convection with near-surface reflectivity
142 < 35 dBZ or precipitation persisting less than 20 min (i.e., poorly-sustained CI events, hereafter
143 referred to as “Fail” events; Fig. 1b), and 3) no observed precipitating convection despite forecasts
144 of CI from an ensemble of convection-allowing WRF simulations (hereafter “Null” events; Fig.
145 1c). For simplicity of naming convention, all heights referenced from the mean sounding launch
146 height will hereafter be referred to as ‘above sea level’ in the model domain (ASL). Composite
147 environments supporting SCI and Fail events have similar convective available potential energy
148 (CAPE; $250\text{--}350 \text{ J kg}^{-1}$), convective inhibition (CIN; $\sim 45\text{--}50 \text{ J kg}^{-1}$), level of free convection
149 (LFC; $\sim 1.7\text{--}1.9 \text{ km ASL}$) for lifted surface parcels, with slightly different equilibrium levels (ELs;
150 7.8 km ASL for Fail and 8.6 km ASL for SCI), and similar free tropospheric RH (mean RH of
151 $\sim 28\%$)(Fig. 1a, b). The Null environment has greater CAPE ($\sim 1100 \text{ J kg}^{-1}$), slightly less CIN (33
152 J kg^{-1}), comparable lifting condensation level (LCL; $\sim 1.2 \text{ km ASL}$), slightly lower LFC ($\sim 1.3 \text{ km}$
153 $\text{ above launch height}$), higher EL ($\sim 10.8 \text{ km ASL}$), and drier free tropospheric RH (mean RH of
154 $\sim 10\%$)(Fig. 1c)².

160 Our overall modeling strategy was designed to examine sensitivities of CI to the interaction
161 between storm-scale updrafts and the near-cloud environment. Several studies indicate the impor-
162 tance of a variety of complex meso-beta-scale phenomena to orographic CI such as the presence
163 of a low-level jet, complex terrain structure, or lee-side flow convergence zones (e.g., Banta 1984;

²The specific values reported here for the SCI, Fail, and Null soundings are different from those reported by Nelson et al. (2021), as we reference them from the composite sounding itself and not the mean across all of the soundings.

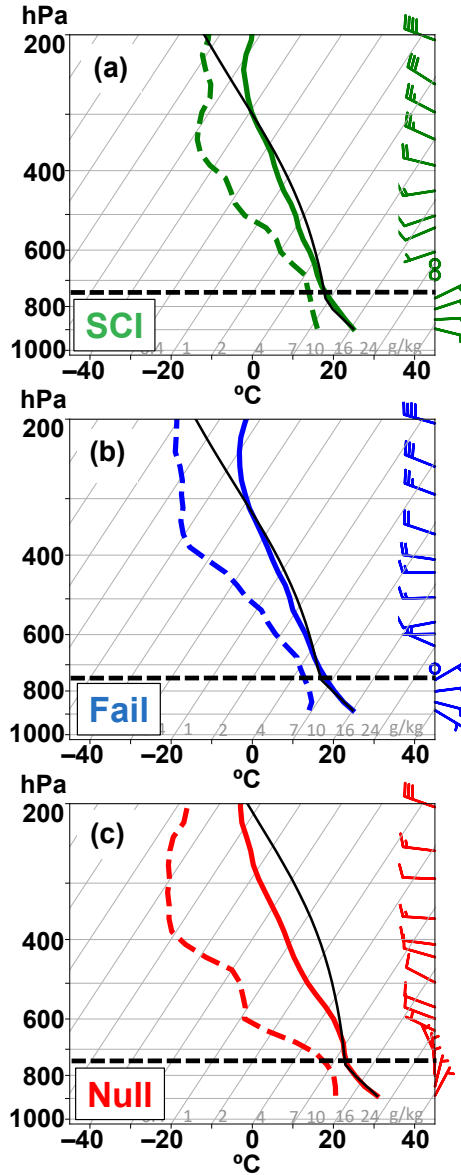


FIG. 1. Mean soundings representative of (a) SCI (green), (b) Fail (blue), and (c) Null (red) events, adapted from Nelson et al. (2021). The mean temperature is the solid line, mean dew point temperature is the dashed line, and the mean surface-based parcel is the solid black line. The mean horizontal wind for each event type is plotted as wind barbs on the right of each panel. The horizontal dashed line in all panels denotes the approximate peak terrain height.

Banta and Schaaf 1987; Behrendt et al. 2011; Hagen et al. 2011; Kirshbaum and Wang 2014; Soderholm et al. 2014; Mulholland et al. 2020; Marquis et al. 2021; Singh et al. 2021). Though our use of soundings synthesizing several convective event types is similar to other deep convective

modeling studies (e.g., Coffer and Parker 2017), it is worth noting that CI may be sensitive to specific details of the environments in individual cases (e.g, the three-dimensional variability of boundary layer properties, capping inversions, sharp wind shear layers, etc.). Assumptions employed in our model design aimed to simplify the interpretation of salient cloud-scale processes common to a variety of observed CI environments while reducing computational requirements for a suite of LES experiments.

a. Updraft thermal tracking

To quantify cloud properties in our experiments, we tracked (in space and time) ensembles of individual moist thermals comprising updrafts occurring in each simulation within ± 15 min of the onset of surface precipitation. To do so, we used an algorithm similar to one used by Peters et al. (2019) that leverages prior methods by Sherwood et al. (2013) and Hernandez-Deckers and Sherwood (2016). At each output time (saved every 5 s during this 30-min window), we identified the local vertical velocity (w) maxima exceeding 3 m s^{-1} within 500 m in all Cartesian directions. Each detected maxima was labeled as a ‘thermal center candidate’ (TCC), whose center is tracked forward and backward in time by matching it with the closest TCC at adjacent time steps within a three-dimensional cone predicted by the expected ascent rate (see Peters et al. (2019) for more details). If the algorithm yielded the same matching TCCs going forward and backward in time, then they were considered to be part of the same thermal track. Resulting thermal tracks with less than three data points were removed. The thermal volume was defined as a spherical region centered at the TCC who’s average w is equal to that of the TCC’s ascent rate.

Using these tracks we cataloged a variety of thermal characteristics in each model run, including updraft size (mean and 90th) percentile thermal width among ensembles occurring in each simulation), thermodynamic properties, and vertical momentum forcings. The vertical momentum budget of a thermal may be written as (e.g., Peters et al. 2019):

$$\frac{dW}{dt} = \{B\} - \left\{ \frac{1}{\rho} \frac{\partial p'}{\partial z} \right\} + m, \quad (3)$$

where W is the thermal’s ascent rate, $B \equiv g \left[\frac{\theta'}{\theta_0} + \left(\frac{R_v}{R_d} - 1 \right) r'_v - r_c \right]$ is the definition of buoyancy in CM1, θ is potential temperature, r_v is the water vapor mixing ratio, r_c is the total condensate mixing ratio, $-\frac{1}{\rho} \frac{\partial p'}{\partial z}$ is the vertical perturbation pressure gradient acceleration (VPGA), and M represents

momentum entrainment. Primes denote local departures from the initial model profiles (denoted by the subscript 0) of a given variable and $\{\}$ represents an average within the thermal's volume. The VPGA term contains information about both dynamically-driven pressure contributions related to the updraft interacting ambient wind shear, as well as buoyancy pressure contributions influenced by both the shape, size, and magnitude of positively buoyant thermals (Tarshish et al. 2018; Peters et al. 2019; McKim et al. 2020). Past studies have shown that m has a relatively small effect on W (Sherwood et al. 2013); therefore, we neglected this term. Using this framework, we calculated mass-flux-weighted mean B and VPGAs across thermals. The volumetric mass flux M is defined at a given height as:

$$M = \sum WV\rho, \quad (4)$$

where \sum represents a sum over all thermals at a given height, and V is the thermal volume. Finally, we estimated the concentration of boundary layer air comprising each thermal by tracking the concentration within them of a passive tracer field that is defined at the time of model initialization to a value of 1.0 within the lowest 2 km ASL of the atmosphere and 0.0 above it. We examined vertical gradients of this field as an analog metric for dilution of thermals by entrainment, which was easily performed for a large number of simulations with computational affordability relative to other more direct methods of measuring entrainment.

3. Terrain-inclusive simulations

A simulation employing the Null base state environment (Fig. 1c) demonstrates that an anabatic mesoscale orographic upslope flow and a deepening dry convective boundary layer naturally begin to develop within 20 min of model initialization (Fig. 2a, d). By $t = 60$ min, +1–2 K magnitude and ~ 1 km-deep boundary layer thermal perturbations consolidate near the terrain peak, yielding an approximately 5-km-wide swath of horizontal wind convergence (Figs. 2c, f, 3b). Thus, a thermally-forced orographic circulation resembling past studies (e.g., Demko and Geerts 2010; Kirshbaum 2011, 2013, 2017, 2020; Kirshbaum and Wang 2014; Soderholm et al. 2014; Mulholland et al. 2020) provides a mesoscale region of convergence and lift, through which humid boundary layer thermals ascend into the free troposphere to produce deep convective clouds.

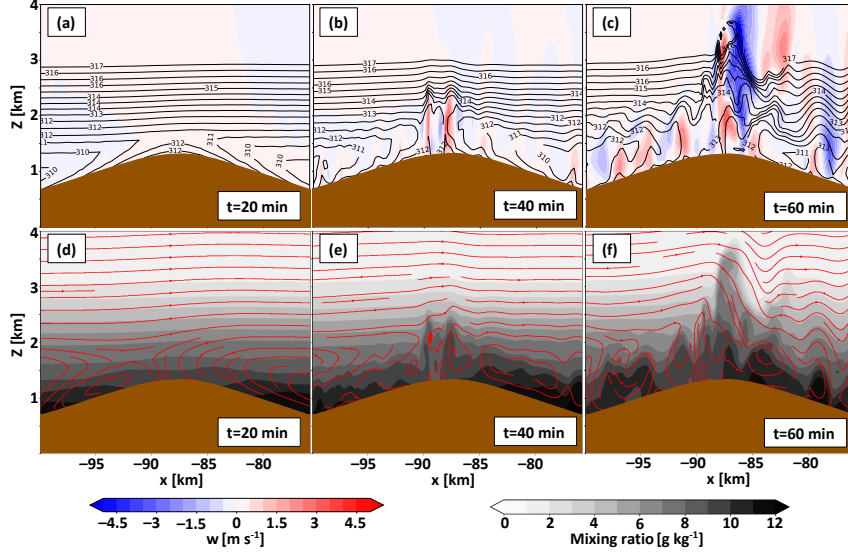


FIG. 2. Evolution of the orographic circulation using idealized terrain, radiation, and surface fluxes. Panels (a–c) show the evolution of vertical velocity (m s^{-1} , shaded) and potential temperature (K, contours). Panels (d–f) show the evolution of mixing ratio (g kg^{-1} , shaded) and streamlines (red).

a. Base SCI, Fail, and Null environments

Our first set of high-resolution simulations applied the horizontally-homogeneous environmental state composed of the composite SCI, Fail, and Null base soundings (Fig. 1). This series of simulations produces precipitation qualitatively resembling the span of observed outcomes during RELAMPAGO-CACTI (Fig. 4). Widespread and sustained precipitation reaches the surface at $t \sim 58$ min in the SCI and Fail environments (Figs. 4a, b, 5a, d, 6a). Although surface precipitation is realized in the base Null run, it is much more isolated, less intense, and first occurs approximately 17 min later than in the base SCI and Fail runs (Figs. 4c, 5g, 6b). Storms forming in the Fail environment are only subtly weaker and less widespread than their SCI counterparts, with similar convective structure and evolution (Figs. 4a, b, 5a–f). Due to the similarities between the SCI and Fail simulations, our remaining analysis compares processes occurring across just the base SCI and Null environments.

In both the SCI and Null simulations, boundary layer parcels ascend to their LFC within the mesoscale orographically-induced updraft. This updraft is advected westward of the terrain ridge-line in the SCI simulation by the low-level easterly upslope flow, similar to past studies (e.g.,

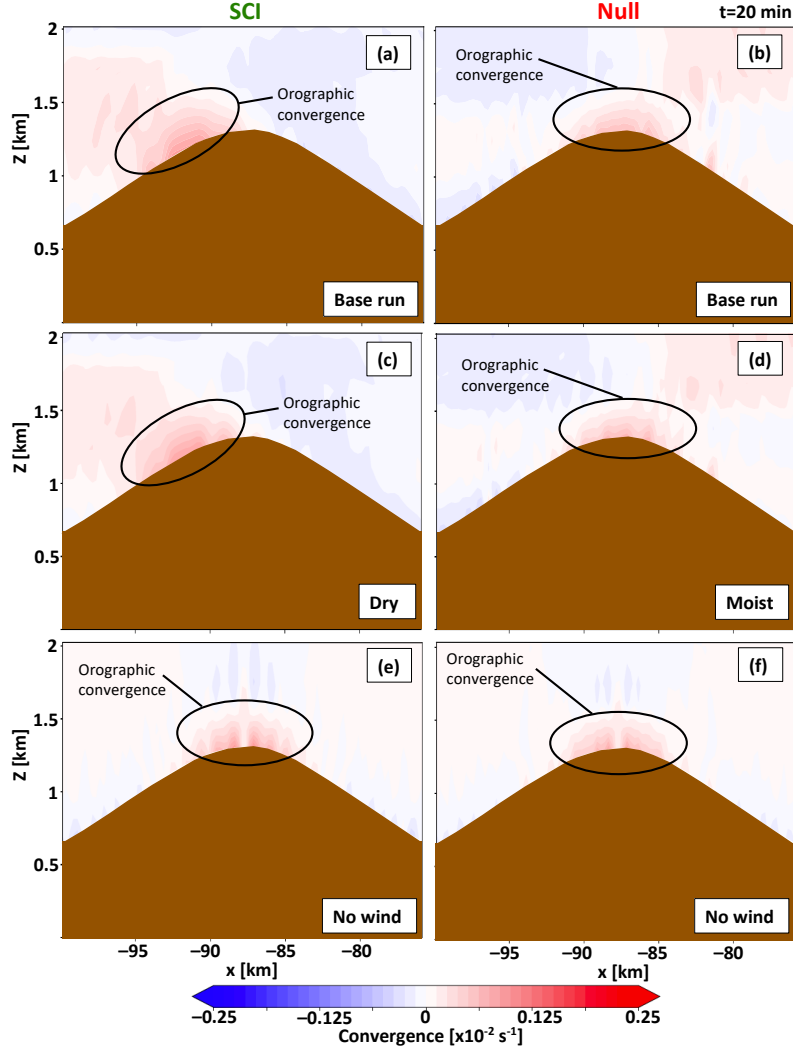


FIG. 3. Convergence (shaded, s^{-1}) at 20 min into the SCI and Null (a, b) base, (c, d) dry/moist, and (e, f) no wind. Convergence (positive values) are shown in red and divergence (negative values) are shown in blue. The E-W cross sections are taken at the same location as those in Figure 5 (denoted by the thick black lines in Fig. 4.).

Kirshbaum and Durran 2004; Kirshbaum 2011, 2013; Wang et al. 2016)(Fig. 5a–c,g–i). Eventually, a chain of rising buoyant thermals produces precipitation rates in excess of 60 mm hr^{-1} in the SCI run (e.g., Fig. 6a). The mesoscale updraft in the Null simulation is located nearer to the ridgeline (or just east of it) because of a weaker cross-terrain flow at low levels (Kirshbaum 2013; Soderholm et al. 2014), but is narrower and shallower than the SCI run, with a weaker

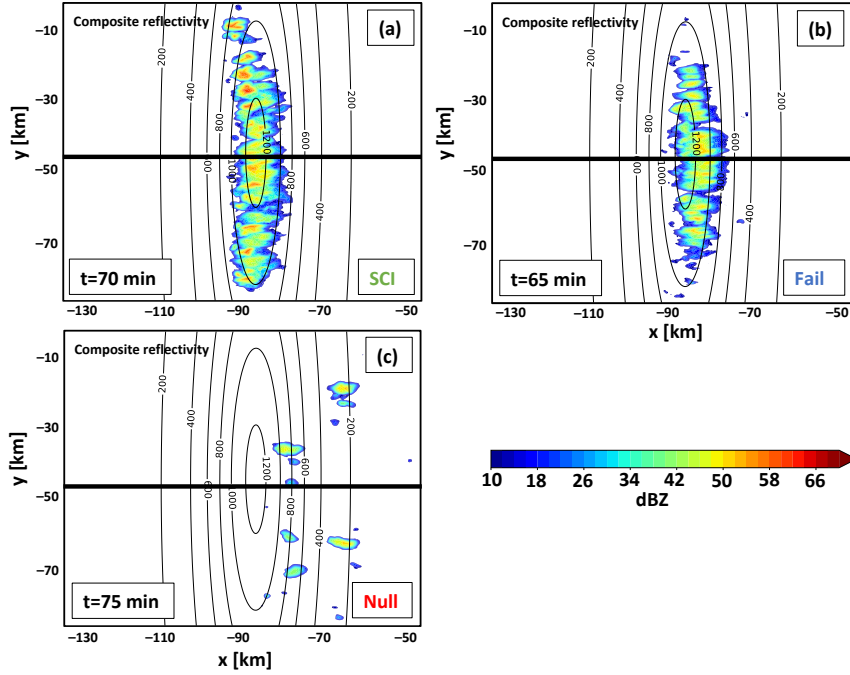


FIG. 4. Composite reflectivity for the (a) SCI, (b) Fail, and (c) Null simulations with idealized terrain, radiation, and surface fluxes. The thick black line denotes the location of E-W cross sections in Figure 5.

orographic circulation and surface convergence (Figs. 3a, b, 5b, h). Shallower convection and smaller precipitation rates ($< 10 \text{ mm hr}^{-1}$) are produced in the Null simulations than in the SCI simulations despite similar peak cloud updraft strengths (Figs. 5b, e, h, 6a, b).

The mean diameter of all tracked thermals for both the SCI and Null simulations is $\sim 1000 \text{ m}$ and $\sim 800 \text{ m}$, respectively (Fig. 7a). Although the mean width of all tracked thermals is only slightly larger in the SCI than in the Null simulations, the diameters of widest updrafts (e.g., 90th percentile in radius among the ensemble of updrafts produced in each simulation) in the SCI run are approximately 800 m greater than in the Null run (at $z < 4 \text{ km}$ above the terrain peak; hereafter ‘ATP’³; Fig. 7a). The ensemble of thermals produced in the SCI simulation has a significantly larger domain averaged volume mass flux due to both the size and number of updrafts, greater mass flux weighted buoyancy at low levels, and experiences a smaller downward VPGA, particularly in at $z < 2 \text{ km ATP}$ (Fig. 7b–d). At $z > 3 \text{ km ATP}$, the few surviving Null thermals have greater buoyancy than the SCI thermals, owing to the larger CAPE in the environment (Fig. 7c). However, they also

³Note that ATP is different from ‘above ground level’ (AGL), as ATP is height relative to a constant reference point ($z = 1.25 \text{ km ASL}$) and AGL is height above the ground, which is a non-constant height. When at $h = 1.25 \text{ km ASL}$, then AGL is the same as ATP.

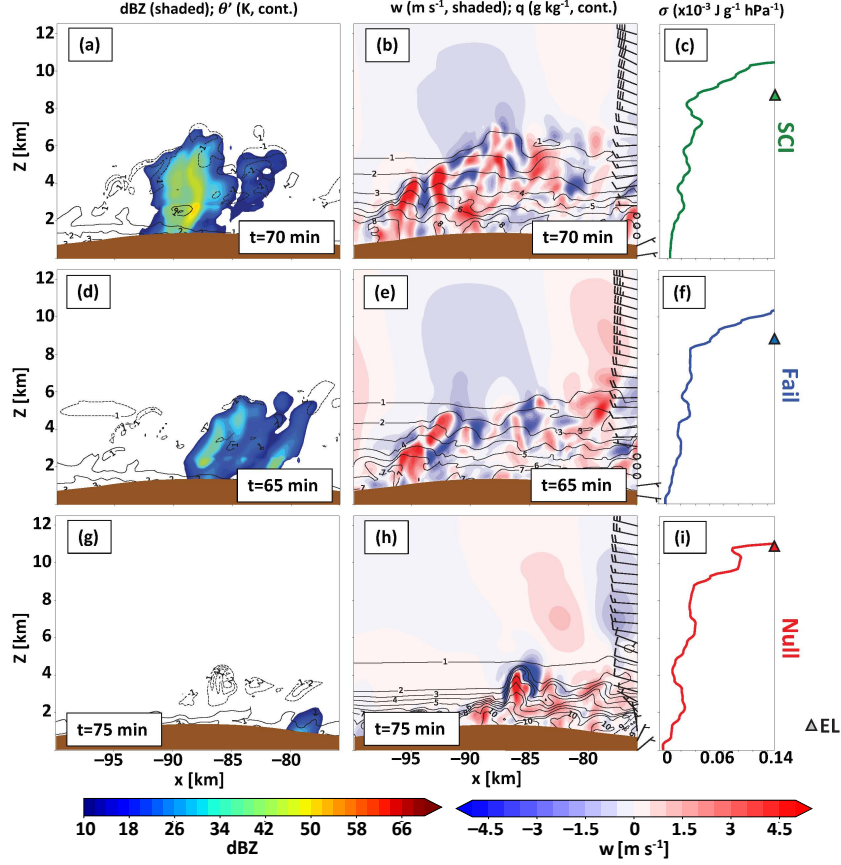


FIG. 5. Cross sections of the (a–c) SCI, (d–f) Fail, and (g–i) Null simulations. All cross sections are E–W across the maximum peak of the terrain (thick black line in Fig. 4). Panels (a, d, g) are reflectivity (dBZ, shaded) and potential temperature perturbation (K, contours). The heights of the environmental EL (triangles on the right-most axis) are representative of a surface-based parcel at the terrain peak 10 min before CI. Panels (b, e, h) are vertical velocity (m s^{-1} , shaded) and mixing ratio (g kg^{-1} , contours). Panels (c, f, i) show the static stability of the initialized sounding. Included in the right-side cross sections (b, e, h) are the horizontal winds (barbs, right-hand axes).

have significant downward-oriented VPGAs (Fig. 7d). As a result, SCI thermals experience a net upward acceleration; whereas, the Null thermals experience a net downward acceleration.

The mean slopes with height of the boundary layer air concentration in both the Null and SCI thermals are similar (Fig. 7e), suggesting that the entrainment rate of ambient air into the thermals also is similar across the environments. Therefore, the buoyancy of thermals in the Null simulation experience larger buoyancy dilution rates than their SCI counterparts over time because of the drier

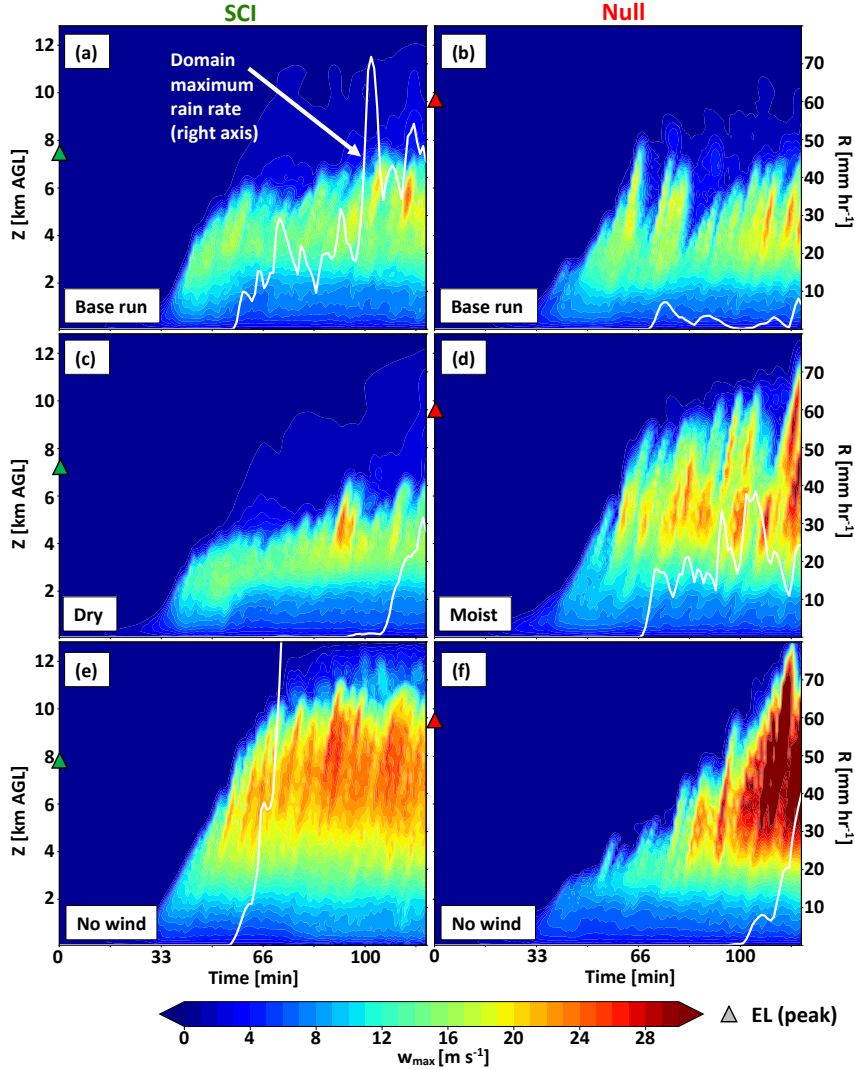


FIG. 6. Hovmöller diagrams of domain-wide maximum vertical velocity as a function of time and altitude (m s^{-1} , shaded, left-axis) and rain rate as a function of time (mm hr^{-1} , white line, right-axis) for the (a, b) base SCI and Null, (c, d) dry SCI/moist Null, and (e, f) SCI and Null with no wind simulations including terrain, radiation, and surface fluxes. The ELs, denoted with triangles on the left hand axes, are representative of a surface-based parcel at the top of the terrain 10 min before CI.

free troposphere. This increased dilution rate is consistent with the smaller net concentration of boundary layer air transported and detrained into the middle free troposphere and considerably higher evaporation rate of cloudy air over time in the Null simulation than in the SCI counterpart (e.g., $z = 4\text{--}8$ km AGL in Fig. 8a, b). Entrainment-driven dilution of Null clouds may be particularly effective owing to their largest updrafts being generally smaller and weaker surface convergence

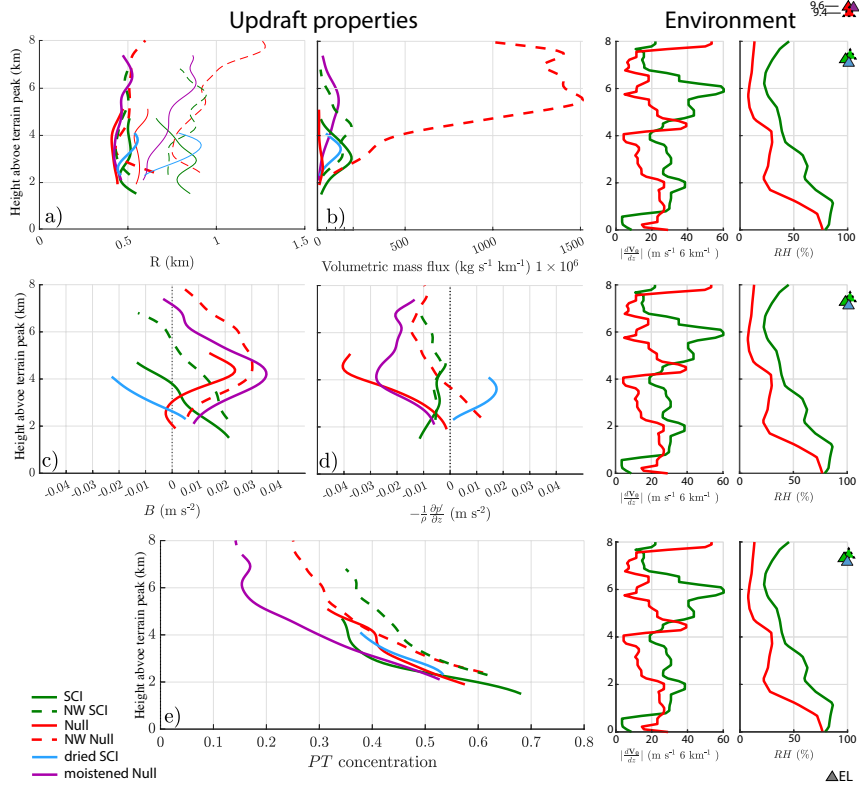


FIG. 7. Tracked thermal characteristics for the base SCI (green, solid), base Null (red, solid), SCI NW (green, dashed), Null NW (red, dashed), dry CI (blue, solid), and moist Null (purple, solid) runs. Panel (a) shows the mean (thick) and 90th percentile (thin) thermal radii. Panel (b) shows the volumetric mass flux, panel (c) shows the thermal buoyancy, panel (d) shows the VPGA, with downward being negative, and panel (e) shows the boundary layer passive tracer concentration as a function of height (in km ATP). Environmental profiles of wind shear and relative humidity are shown to the right. The EL representative of surface-based parcels from the peak of the terrain are provided triangles on the right axis. The ELs for the Null simulations are off-axis, but are shown relatively at the top of the plot.

supporting them than in the SCI environment (Figs. 3, 7). The higher dilution rate and adverse VPGAs aloft decrease the amount of precipitation that can be generated in the Null simulation and prevent them from reaching greater altitudes than the SCI thermals despite the Null environment having a much higher EL.

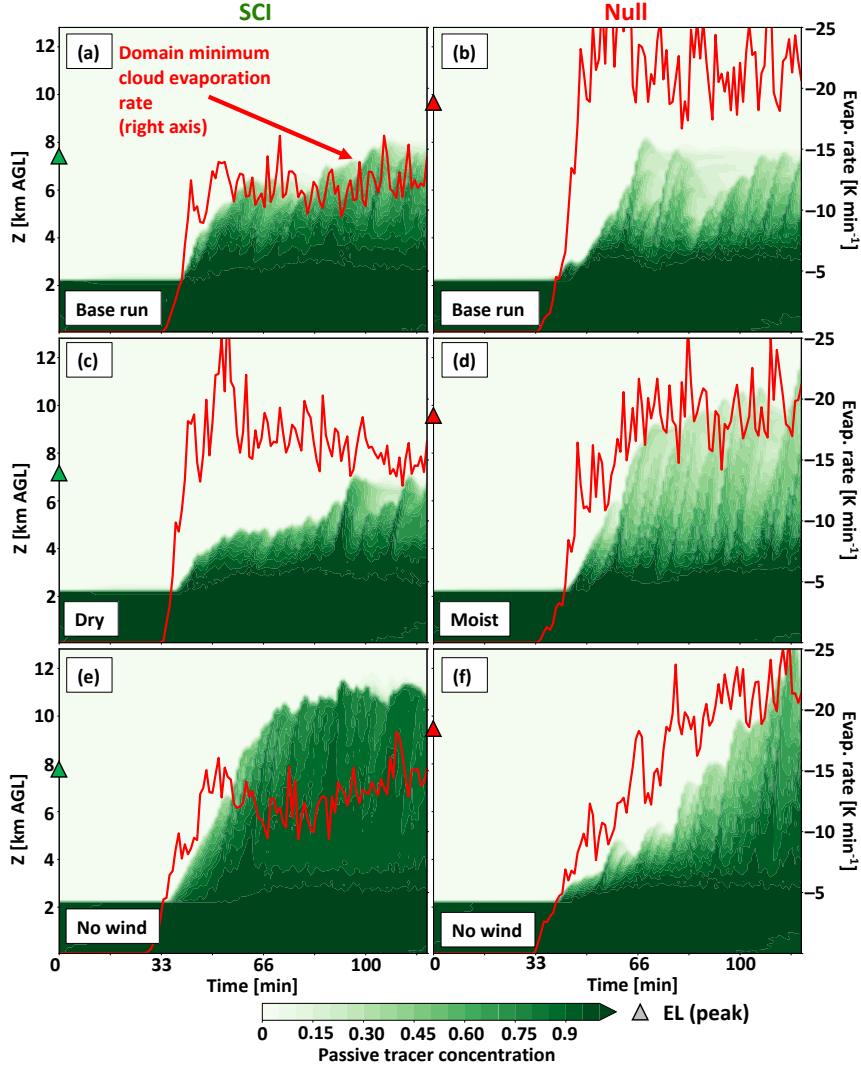
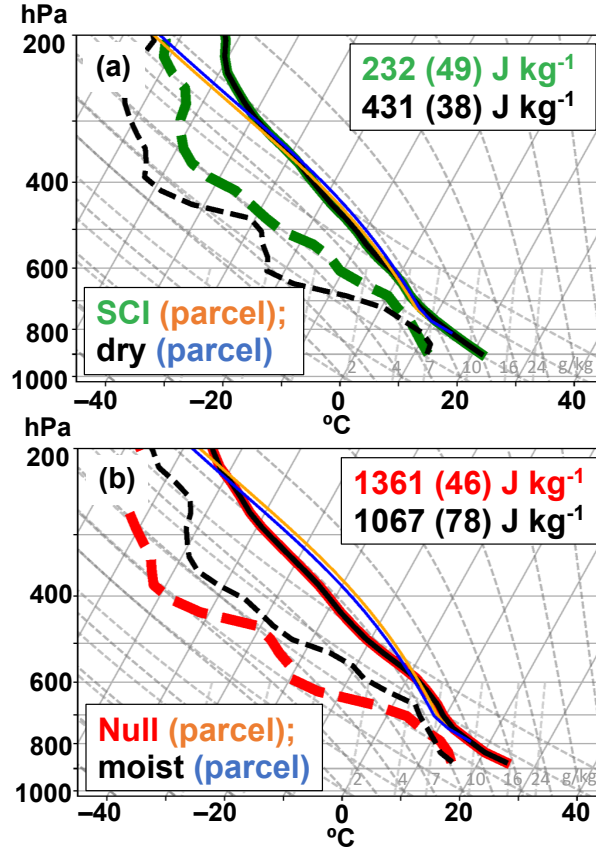


FIG. 8. Same as Figure 6, but of maximum boundary layer passive tracer (shaded, left-axis) and cloud evaporation rate (K min^{-1} , red line, right-axis).

b. Relative humidity experiment

To test a hypothesis posed by Nelson et al. (2021), we performed an experiment examining the sensitivity of CI outcome to the observed moisture conditions. We employed the same model and base state configuration as in section 3a; however, we modified the base SCI and Null environments by swapping their dew point depression profiles. This has the effect of moistening the free troposphere in the Null thermodynamic environment and drying it in the SCI environment (Fig. 9). We posed this experiment to test if CI could have occurred in the observed Null environments if it

306 had a similar moisture profile as that in the observed SCI environments. For naming convention, we
 307 refer to the swapped humidity profile simulations as “moistened Null” and “dried SCI”. However,
 308 we note that simply swapping these moisture profiles results in a subtle drying of the Null boundary
 309 layer and moistening of the SCI boundary layer. This alters values of CAPE, CIN, and other metrics
 310 relevant to CI for low-level mean-layer (ML) parcels (Fig. 9). These ramifications are discussed
 311 below.



312 FIG. 9. Modified SCI and Null soundings, where (a) the SCI sounding (green) is dried using the Null dew point
 313 depression (black), and (b) the Null sounding (red) is moistened using the SCI dew point depression (black).
 314 Lifted parcels representative of the mean of the lowest 100-hPa-deep layer of the sounding (‘ML’ parcel) are
 315 shown for the base soundings (orange) and the modified soundings (blue). ML CAPE (ML CIN) is provided for
 316 each sounding in the top right corner.

317 The dried SCI environment produces shorter updrafts (by ~2 km), dramatically reduced precip-
 318 itation rates (by 50% or more), and cells that are more isolated than in the base SCI experiment
 319 (c.f., Fig. 6a, c). Further, precipitation formation is delayed, beginning at $t = 100$ min versus $t =$

60 min in the base SCI run (Fig. 6a, c). In contrast, the moistened Null environment produces convection akin to the base SCI run, but with deeper and stronger updrafts, and only slightly delayed and weaker precipitation rates than in the base Null or base SCI environments (c.f., Fig 6a, d). Mean thermal width in the moist environments (base SCI and moistened Null) is not significantly different from the dry counterpart environments (dried SCI and base Null); yet, volume mass flux is larger in the moist simulations owing to more numerous and stronger updrafts, and the widest updrafts (e.g., 90th percentile radius) being even wider (Fig. 7a, b). Entrainment rate throughout the depth of the moist environment updrafts is not appreciably different than for thermals in the base environment experiments (Fig. 7e).

Mean thermal buoyancy is consistently more positive in the moist environments than in the dry ones, a result of reduced buoyancy dilution by comparatively more humid free tropospheric air. As mentioned above, a ML parcel lifted in the dried SCI environment, has slightly greater CAPE and lower CIN than the base SCI environment, while a ML parcel lifted in the moistened Null profile has slightly less CAPE and more CIN than the base Null environment (Fig. 9). Because these ML parcel CAPE and CIN changes might be expected to lessen buoyancy of low-level updrafts produced in the moistened Null run and promote them in the dried SCI run (the opposite outcome of what is simulated), the results suggest that updraft buoyancy characteristics are quite significantly altered by dilution with their free tropospheric surroundings in these simulations. This conclusion is further supported by the general decrease in evaporation rate of cloudy air from the base Null simulation to the moist Null simulation and increase in evaporation of cloudy air from the base SCI run to the dried SCI run (Fig. 8a–d).

There was no alteration of the base state wind profiles in this experiment, so the magnitude of the low-level orographic convergence near the time of CI is not substantially altered (c.f., Figs. 3a, b and 3c, d). As in the base SCI simulation, the moistened Null simulation yields a long-lasting orographically-driven mesoscale updraft through which boundary layer thermals ascend into the free troposphere. Whereas, sustained deep updrafts emerging from the orographic circulation do not occur in the dried SCI environment until much later ($t = 90\text{--}100$ min; Fig. 6c). Though the Null environments had slightly greater static stability near the top of the boundary layer, moistening the free troposphere of the base Null profile helps updrafts overcome the larger CIN. The moist Null simulation also has a smaller cloud evaporation rate compared to the base Null, suggesting

that the negative effects of entrainment are abated when moistening the free troposphere (Fig. 8b, d). Altogether, these results suggest that if the observed Null environments were not as dry, then perhaps deep convection may have been deeper and stronger than in the base SCI environment because of the larger ELs and CAPE.

c. Wind variation experiment

To explore the relative effects of the background wind on cloud-scale updraft processes (e.g., shear suppression effects) and the mesoscale orographic circulation, we conducted a variety of sensitivity experiments altering the base SCI and Null wind profiles. With the background wind profile set to zero (i.e., no wind; hereafter ‘NW’), precipitating convection in the NW SCI environment occurs at approximately the same time and geographical location as in the base SCI run, except with stronger updrafts and a greater precipitation rate (by a factor of ~ 1.5 and 3, respectively; Fig. 6a, e). Thus, removal of the background low-level easterly wind (and corresponding upslope flow on the east side of the terrain), does not hinder the development of convection.

The maximum updraft strength attained in the NW Null environment is diminished between $t = 30$ – 65 min relative to the base Null environment, a result of the relatively strong static stability atop the boundary layer that caps the ascent associated with the solenoidal terrain circulation (Figs. 1c, 3, 5i). Further, this terrain circulation is slightly weaker in the absence of a background mesoscale low-level flow (c.f., Figs. 3b, f, 5g–i). However, NW Null peak updrafts are considerably stronger and deeper at $t > 65$ min ($> 28 \text{ m s}^{-1}$ and 2–4 km, respectively), with more widespread precipitation than the base Null profile and stronger updrafts than in the base or NW SCI runs (Fig. 6a, b, e, f). These stronger updrafts develop partially because by this time there is enough convergence and buoyancy near the terrain peak to reduce the capping inversion, allowing sufficiently developed boundary thermals to enter the free troposphere (e.g., Fig. 2). The suppressing effect of the cap is not as oppressive early in the base Null run because of the inclusion of low-level upslope flow. Further, despite having comparable low-level convergence magnitude, the inclusion of wind yields greater elevated convergence (e.g., $z > 1.5 \text{ km ASL}$) east of the peak in the base Null run compared to the NW Null run (Fig. 3b, f), perhaps analogous to the behavior of convergence in varying wind profiles shown by Hagen et al. (2011). The nature of the orographic flow is significantly different between the base and NW SCI experiments. The area of convergence is shifted eastward to the

379 ridgeline and is shallower in the NW SCI run compared to the base SCI (Fig. 3a, e); though, the
380 depth of convergence AGL is similar. Ultimately, updrafts from both the NW SCI and Null NW
381 simulations reach their ELs, unlike their base SCI and Null environment counterparts, yielding
382 larger overall vertical mass flux at $z > 3$ km ATP, particularly in the NW Null environment (Figs.
383 6e, f, 7b).

384 Diameters of the largest thermals (90th percentile) are 500–600-m larger in the NW Null environ-
385 ment than the base Null environment (Fig. 7a). However, there is not a comparable difference in
386 thermal width between the base and NW SCI simulations; conversely, the widest NW SCI thermals
387 are slightly narrower than those in the base SCI run (at $z < 4$ km ATP; Fig. 7a). Thermals in
388 both NW SCI and Null simulations contain larger mean buoyancy than their base SCI and Null
389 counterparts (Fig. 7d). The large positive buoyancy is tied to a reduced entrainment rate in the free
390 troposphere, as evidenced by the reduced decay of the passive boundary layer tracer concentration
391 at $z > 4$ km ATP (Fig. 7e). This inferred entrainment rate is less than in either the base or moistened
392 Null or dry SCI simulations, suggesting that entrainment and dilution rates are reduced in a calm
393 environment. However, NW Null thermals still appear to suffer greater dilution and cloud water
394 evaporation rate (Fig. 8e, f) over their full depths than NW SCI thermals, similar to the base
395 simulations, because of the drier free troposphere in the Null profile.

396 1) OTHER WIND PROFILE SENSITIVITY SIMULATIONS

397 To further determine if differences in CI outcome are sensitive to each base wind profile, we
398 performed an additional simulation utilizing an environment composed of the base Null thermo-
399 dynamic and moisture profile, but prescribed the base SCI wind profile. Isolated and transient
400 precipitating cells initiate late in the simulation ($t = 105$ min), delayed approximately 45 min from
401 initiation in the base Null run and approximately 10 min from the Null NW run (Fig. 10a, b,
402 d). Maximum updraft height is significantly suppressed in this scenario (Figs. 10a, b, 11a, b),
403 in part from stronger opposing shear-induced VPGAs within the free troposphere, but also from
404 recharacterization of the low-level winds to include stronger cross-terrain flow such that the accu-
405 mulation of buoyancy near the ridgeline is disrupted (e.g., Hagen et al. 2011; Kirshbaum 2011,
406 2013). Further, while this Null simulation with the SCI wind profile has higher boundary layer
407 tracer concentration within thermals at $z < 4.5$ km AGL, there is a rather sharp vertical gradient in

the concentration and generally weaker cloud water evaporation, suggesting that a combination of adverse VPGAs and changes to low-level convergence rather than enhanced entrainment restricts the growth of deep convection in this simulation (Fig. 11a, b).

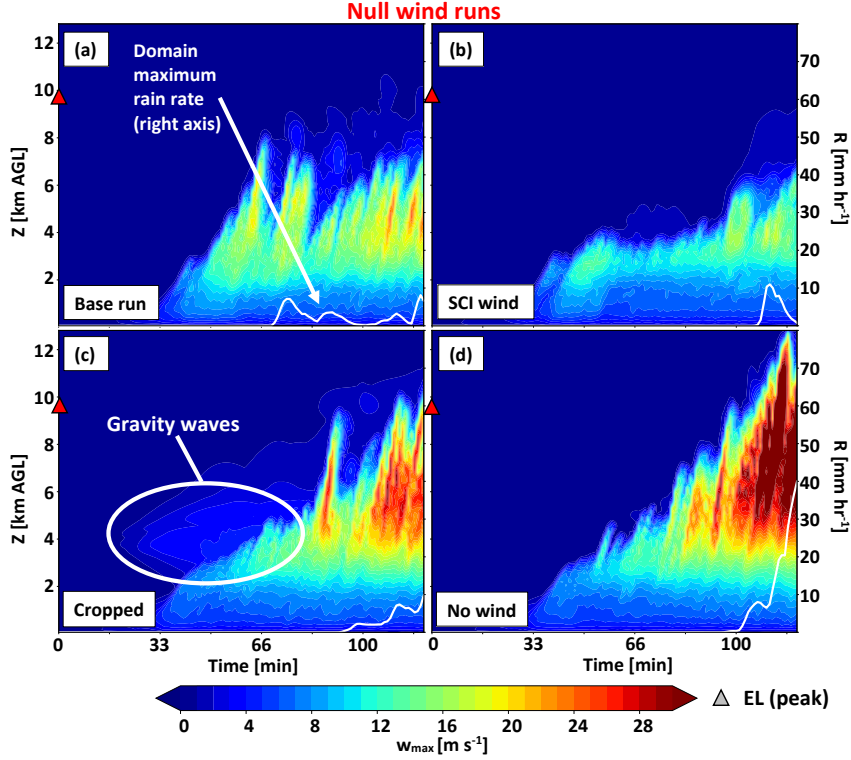


FIG. 10. Same as Figure 6, but for (a) the base Null run, (b) Null with SCI wind, (c) Null with cropped wind below 4 km, and (d) Null with no wind.

A final sensitivity experiment isolated the shear effect occurring within the free troposphere from mechanically-induced ascent along the terrain associated with the low-level background wind. This was done by setting the wind speed in the base Null environment profile to zero at $z < 4$ km ASL (called the ‘cropped’ wind Null run); thereby, allowing the natural thermally-induced orographic circulation in the boundary layer to evolve unmodified by low-level upslope flow. Due to the increased vertical wind shear at $z = 4$ km ASL, near the area of the relatively strong static stability in this simulation, vertically propagating gravity waves were introduced to the mesoscale flow. The wave activity has updrafts with magnitudes strong as $\sim 6 \text{ m s}^{-1}$ between $z = 3\text{--}6$ km ASL and $t = 25\text{--}75$ min that precede the thermals erupting from the boundary layer (Fig. 10c). Generally, the behavior of the convective updrafts in the cropped Null experiment lies between that of the base

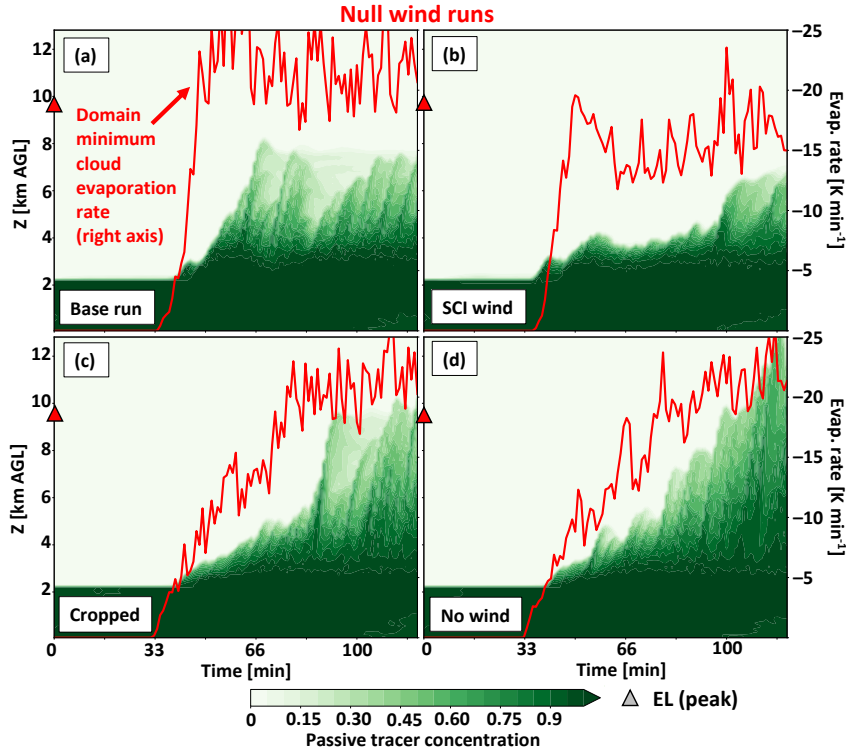


FIG. 11. Same as Figure 10, but of maximum boundary layer passive tracer (shaded, left-axis) and cloud evaporation rate (K min^{-1} , red line, right-axis).

and NW Null experiments (Figs. 10a, c, d, 11a, c, d). Ascending boundary layer thermals are suppressed early in the simulation ($t = 30\text{--}80$ min) compared to the base Null simulation, but reach a greater altitude and magnitude after 80 min. However, updrafts are never as deep or as strong as in the NW Null simulation. This indicates that shear isolated to the free troposphere does have a suppressing effect on the developing updrafts. However, maximum cloud water evaporation rate is comparable among the NW and cropped updrafts, as is the reduction of the concentration of boundary layer air within thermals during their ascent (Fig. 11a, c, d), both suggesting similar thermal dilution rates across these simulations.

Differences in the characteristics of individual ascending thermals in the NW and cropped Null runs may also be sensitive to the details of their encounter with updraft or downdraft branches of the terrain-induced gravity waves. As may be expected, ascent of thermals is generally suppressed upon encountering downdrafts and enhanced upon encountering updrafts associated with the gravity waves. As an upward branch of the wave interacts with the boundary layer thermals comprising the

438 orographic updraft region, convection is enhanced by increasing vertical velocity by $O[1 \text{ m s}^{-1}]$
 439 and increasing the depth of the mesoscale updraft by $O[100\text{-m}]$. Eventually, the orographic updraft
 440 deepens through the wave layer and robust precipitating convection occurs from additional rising
 441 boundary layer thermals at $t \sim 100 \text{ min}$ (Fig. 10c). This moistening may be one reason that updrafts
 442 from the cropped run reach higher altitudes and have stronger maximum updraft strengths than
 443 the base Null run ($\sim 8 \text{ km}$ vs 6 km AGL), but ultimately suffer from entrainment-driven dilution
 444 and negative VPGAs in the dry free troposphere above this layer (Figs. 10a, c, 11a, c). Thus, the
 445 simulation of these gravity waves indicates a scenario in which ascending thermals may not always
 446 be suppressed by strong environmental wind shear.

447 **4. Flat terrain sensitivity tests**

448 Given the prominent role of the terrain on CI in our simulations shown above, we performed a
 449 few additional simulations with no surface fluxes, radiation, or terrain to examine the sensitivity
 450 of CI without the presence of orographically-induced mesoscale ascent. In these experiments,
 451 convective updrafts were initiated by prescribing an individual ellipsoidal temperature perturbation
 452 (i.e., ‘thermal’) within the boundary layer at the model initialization time. The thermals had a
 453 maximum magnitude of $+2 \text{ K}$, and a 1.5 km vertical and 5 km horizontal diameter centered at
 454 0.75 km AGL⁴. These parameters were chosen based on sensitivity experiments testing a variety
 455 of horizontal and vertical thermal diameters ($2.5\text{--}7.5 \text{ km}$, $1\text{--}2 \text{ km}$, respectively) and magnitudes
 456 ($+1\text{--}3 \text{ K}$). Convective structure was most sensitive to the horizontal diameter (not shown). A
 457 thermal width of 5 km was the narrowest thermal producing precipitating convection in the base
 458 SCI environment.

459 Ascent of the prescribed thermal in the base SCI and Null environments yields a singular
 460 precipitating updraft (Fig. 12). The updraft in the flat terrain SCI simulation ascends to $z \sim 5.5$
 461 km AGL, similar to the height ATP achieved in the terrain-inclusive SCI simulation, but falling
 462 short of the EL predicted by lifting a surface parcel from the base-state environment (8.5 km
 463 AGL) (c.f., Fig. 6a and 12a). Although a slightly stronger precipitating updraft is produced in the
 464 Null environment, it reaches a similar height as in the SCI simulation and falls quite short of its
 465 surface-based parcel EL (10.8 km AGL) (c.f., Fig. 6b and Fig. 12b).

⁴Note that AGL is the same as ASL in these flat terrain simulations.

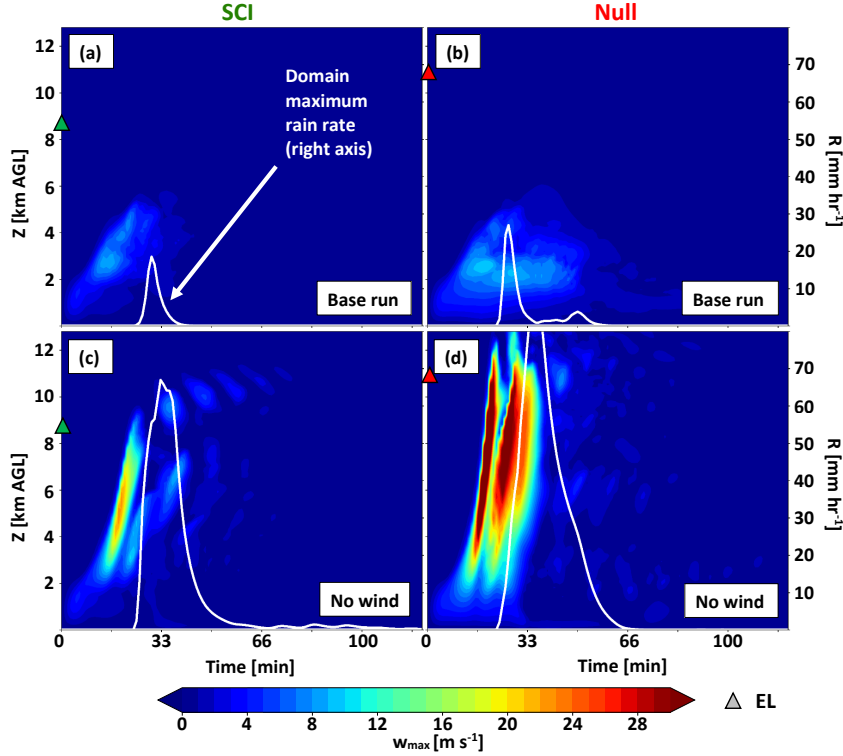


FIG. 12. Same as Figure 6, but for the base (a, c) SCI and (b, d) Null simulations releasing a prescribed thermal with no terrain or surface heat fluxes (a, b) with and (c, d) without wind. Environmental EL are representative for a surface-based parcel at $t=0$ min.

To isolate shear suppression effects upon ascending thermals from the mesoscale orographic circulation, we set the ambient wind profile equal to zero as in the ‘NW’ experiment shown in section 3c (Fig. 12c, d). As in the terrain-inclusive NW simulations, updrafts in the flat-terrain NW SCI and NW Null simulations are stronger, reach their predicted surface-based ELs, and yield generally larger maximum near-surface rainfall (c.f., Fig. 6e, f and 12c, d). Further, the flat-terrain NW Null updraft achieves a similarly intense magnitude as its terrain-inclusive counterparts at $t > 90$ min. Thus, convective updraft behavior occurring in the absence of a mesoscale lifting mechanism further confirms the suppressing effects of vertical wind shear on deepening clouds.

It is important to note that a natural evolution of progressively deepening clouds is not necessarily captured in these simulations. For example, the prescribed thermal in the flat-terrain NW Null simulation rises quite rapidly to its EL; while, a longer period of consolidation of boundary layer buoyancy along the ridgeline is required to generate sustained updrafts in the terrain-inclusive

481 NW Null simulation (c.f., Fig. 6f and 12f). The immediacy of updraft growth in this flat
482 terrain experiment is related to our prescription of a 5-km-wide boundary layer thermal, which is
483 required to achieve precipitating updrafts in the SCI environment. Thus, it is important to exercise
484 caution when employing a prescribed thermal methodology to initiate deep updrafts in convective
485 simulations, especially given the sensitivity of entrainment effects on updraft width (e.g., Morrison
486 2017; Lecoanet and Jeevanjee 2019; Morrison et al. 2020; Peters et al. 2020).

487 5. Discussion

488 Altering the humidity profiles in the free troposphere of the SCI and Null environments had
489 profound effects on entrainment-driven dilution of updrafts. All other parameters left unaltered,
490 a moistened Null free troposphere produced numerous deep updrafts with strong buoyancy and
491 large precipitation rates. Though artificially dried SCI environments still yielded precipitating
492 convection, updrafts were generally less buoyant, shallower, and yielded smaller precipitation rates
493 than the base SCI environment. This supports the hypothesis that entrainment of free-tropospheric
494 dry air alone is a prominent governor of deep CI in the observed RELAMPAGO-CACTI cases,
495 similar to conclusions by other studies using idealized environmental profiles (Crook 1996; Zhao
496 and Austin 2005; Damiani et al. 2006; Houston and Niyogi 2007; Romps 2010; De Rooy et al.
497 2013; Hernandez-Deckers and Sherwood 2016, 2018; Morrison 2017; Moser and Lasher-Trapp
498 2017; Rousseau-Rizzi et al. 2017; Leger et al. 2019; Morrison et al. 2020; Peters et al. 2019, 2020).

499 Results from our experiments suggest somewhat separable impacts of the wind profile upon the
500 character of ascending updrafts and the probability of CI. While clouds interacting with vertical
501 wind shear in the free-troposphere yield opposing (downward-oriented) VPGAs that suppress
502 updrafts (consistent with the findings of Peters et al. (2019, 2021a,b); Morrison et al. (2020); Peters
503 et al. (2020)), changes in the low-level flow affect mesoscale ascent and accumulation of buoyancy
504 realized along the terrain (Kirshbaum 2011, 2013). Past literature sometimes casually implicates
505 shear in the direct modification of entrainment of clouds and updrafts (Markowski et al. 2006;
506 Wang et al. 2008; Markowski and Richardson 2010; Wang et al. 2012). However, other studies
507 show that there may not be a change in the net entrainment rate near thermals ascending in ambient
508 wind shear; rather, entrainment is increased on the downshear side of clouds and decreased on the
509 upshear side (e.g., Zhao and Austin 2005). It is possible that shear may play indirect roles in cloudy

dilution through updraft-suppressing VPGAs that would increase the residence time of individual ascending thermals within the dry free troposphere prior to the production of precipitation. This conclusion may be akin to one made by Markowski et al. (2006), where relatively deep cumulus are fueled by upright sub-cloud inflow trajectories owing to weak ambient wind shear, along which less dilution via entrainment could occur than if trajectories are significantly tilted by stronger shear.

Some recent studies highlight preconditioning of the environment through detrainment of cloudy air from predecessor updrafts within thermal chains as being an important part of the CI process (Damiani et al. 2006; Varble et al. 2014; Hernandez-Deckers and Sherwood 2016; Moser and Lasher-Trapp 2017). Our results indicated some circumstantial evidence that this may have encouraged CI in many of our terrain-inclusive calm wind simulations because the earliest updrafts often were shorter than later ones (Fig. 6a, b, e, f). However, it is not clear if this effect is a necessary condition for CI, because the presence of background wind shear in the base SCI runs yields a cloud-relative and terrain-relative mean wind that may advect moisture away from the geographical region where clouds are deepening. A detailed analysis of the importance of this effect in the context of our numerical experiments is planned as future work.

The greatest sensitivity in thermal width across our experiments was realized by the largest thermals in each simulation, and the overall widest updrafts occurred in the environments with the most significant orographic circulations, consistent with Hernandez-Deckers and Sherwood (2016) and Rousseau-Rizzi et al. (2017). Mean thermal radius was not significantly different across our terrain-inclusive experiments (differences were $< 0.1\text{--}0.2$ km); however, the largest simulated updrafts in our experiments were $\sim 0.2\text{--}0.4$ km wider in the most humid and calm environments versus drier or sheared environments. Based on the comparisons between our terrain-inclusive and flat-terrain experiments (sections 3 and 4, respectively), the orographic mesoscale updraft appeared to play a key role in allowing thermals that spatially scale with the depth of the boundary layer ($\sim 1\text{--}2$ -km diameter) to achieve CI. It was necessary to prescribe much wider thermals in the flat-terrain simulations in order to achieve CI. Observed thermal sizes may not be the same across the three observed event types owing to complex mesoscale environments. For example, thermals associated with Fail or Null events may be smaller and/or weaker than in SCI events, making them less able to withstand buoyancy dilution by entrainment. This is perhaps consistent

540 with our measurements of updraft width across our base SCI and Null simulations (90th percentile
541 radii measurements in Fig. 7a), and may be consistent with dual-Doppler observations of low-level
542 updraft size across differing CI outcomes (Marquis et al. 2021).

543 6. Summary

544 We conducted a series of storm-scale LES employing horizontally-homogeneous base states
545 composed of radiosonde profiles supporting a variety of deep CI outcomes observed along the
546 Sierras de Córdoba range in central Argentina during the RELAMPAGO and CACTI field cam-
547 paigns. Our goal was to relate specific convective updraft processes associated with successful and
548 unsuccessful CI outcomes to the surrounding environmental shear, moisture, and orographically-
549 induced mesoscale flow. We tracked convective updraft width, depth, strength, and processes
550 modulating them, such as thermal buoyancy, inferred entrainment and dilution rates, and opposing
551 vertical pressure gradient accelerations across 13 simulations that utilize composite observed envi-
552 ronments and variations upon them as initial conditions. Experiments comparing the simulations
553 supported the following conclusions:

- 554 1. Thermally-induced orographic ascent aided the ascent of 1–2-km-wide boundary layer buoyant
555 thermals to their LFCs during the CI process. Without this focused mesoscale convergence
556 and ascent, much wider (~5-km-diameter) boundary layer thermals were required to yield CI.
- 557 2. Altering the humidity profiles in the free troposphere of the SCI and Null environments had
558 a profound influence on CI. The entrainment of free-tropospheric dry air was a salient factor
559 governing maximum updraft depth and buoyancy in the RELAMPAGO-CACTI environments.
- 560 3. Though the maximum achievable depth of convection was quite sensitive to the free tropo-
561 spheric shear, the ability for boundary layer thermals to reach their LFC was highly sensitive
562 to the low-level winds that alter the character of orographic mesoscale ascent.
- 563 4. Though mean thermal radius was not significantly different across our terrain experiments,
564 the largest simulated updrafts in our experiments were ~0.2–0.4 km wider in the most humid
565 and calm environments.

566 Collectively, our findings confirm that both wind and moisture profiles are key factors in the CI
567 process. Specifically, the combined effects of: adverse VPGAs (via vertical wind shear), terrain-

568 flow interactions (via upslope flow and organized mountain top convergence), and strength of
569 thermal buoyancy dilution (via dry air entrainment), dictated the probability of CI. However, it was
570 not always possible to clearly disentangle the effects of shear from moisture variation on thermal
571 width and buoyancy, opposing pressure gradient forces, and entrainment processes because many
572 of these processes feedback on each other. For example, if the primary suppressing effect of shear
573 is to yield downward-oriented VPGAs that oppose ascending thermals, this would be expected
574 to increase the exposure period of clouds to entrainment of dry free tropospheric air before they
575 can effectively generate precipitation. A more complete disentanglement of the relative roles of
576 boundary layer and free tropospheric shear on updrafts was complicated by the introduction of
577 terrain-induced gravity waves.

578 It was our primary goal to better understand how cumulus updrafts interact with the ambient near-
579 cloud environment under somewhat simplified and controlled conditions (e.g., initial environmental
580 horizontal homogeneity and omission of the background synoptic conditions). Our experimental
581 design provided some clues to the relative roles of the ambient wind interacting directly with the
582 cloud and also with the terrain to affect the local mesoscale orographic circulation. However, it is
583 important to acknowledge that our relatively idealized model design likely underrepresents realistic
584 orographically-induced convergence originating from its interaction with complex heterogeneous
585 flow, such as lee-side flow convergence regions often observed and simulated in mountain convec-
586 tion scenarios. Future cloud-scale LES should consider these complicated mesoscale conditions
587 in relation to updraft interactions with the near-cloud environment.

588 Domain mean volume mass flux increased in our simulations in which calm winds are pre-
589 scribed (compared to those with the composite environmental wind profiles prescribed) owing
590 to modification of orographic convergence. Wind shear would also be expected to increase the
591 cloud-relative wind field, which may also increase the vertical mass flux per individual updraft.
592 Ongoing work by the authors further examines this concept in detail (e.g., Peters et al. 2021a,b).
593 Finally, given the importance of updraft width on the ultimate CI outcome, it is important to better
594 understand the initial controls of updraft width at low levels. In particular, future work should
595 focus on understanding the environmental factors controlling the width of boundary layer thermals
596 as they transition through the boundary layer cap and into the free troposphere, particularly in the

context of realistic mesoscale forcing mechanisms like the thermally-induced orographic circulation examined in this study.

Acknowledgments. T. Connor Nelson's, James N. Marquis', and Katja Friedrich's work was supported by NSF grants AGS-1661707 and by the U.S. Department of Energy's of Science Biological and Environmental Research as part of the Atmospheric System Research program. John Peters' work was supported by NSF grants AGS-1928666, AGS-1841674 and DOE-ASR grant DE-SC0000246356. Pacific Northwest National Laboratory is operated by Battelle for the U.S. Department of Energy under Contract DE-AC05-76RLO1830. Simulations were performed using George Bryan's CM1 model on NCAR's Cheyenne supercomputing facility. Thank you to CISL for supporting these computing activities. We also are thankful for helpful discussions with Adam Varble, Jake Mulholland, Zhe Feng, George Bryan, Nicholas Luchetti, Steve Nesbitt, Itinderjot Singh, Hugh Morrison, and to participants of the RELAMPAGO and CACTI field project for your dedication to collecting the radiosonde data used in this study.

References

- Banta, R., 1984: Daytime boundary-layer evolution over mountainous terrain. Part 1: Observations of the dry circulations. *Mon. Wea. Rev.*, **112**, 340–356.
- Banta, R., and C. B. Schaaf, 1987: Thunderstorm genesis zones in the Colorado Rocky Mountains as determined by traceback of geosynchronous satellite images. *Mon. Wea. Rev.*, **115**, 463–476.
- Behrendt, A., and Coauthors, 2011: Observation of convection initiation processes with a suite of state-of-the-art research instruments during COPS IOP 8b. *Quart. J. Roy. Meteor. Soc.*, **137**, 81–100, <https://doi.org/10.1002/qj.758>.
- Bryan, G. H., and M. J. Fritsch, 2002: A benchmark simulation for moist nonhydrostatic numerical models. *Mon. Wea. Rev.*, **130**, 2917–2928.
- Coffer, B. E., and M. D. Parker, 2017: Simulated supercells in nontornadic and tornadic VORTEX2 environments. *Mon. Wea. Rev.*, **145**, 2917–2928, <https://doi.org/10.1175/MWR-D-16-0226.1>.
- Crook, N. A., 1996: Sensitivity of moist convection forced by boundary layer processes to low-level thermodynamic fields. *Mon. Wea. Rev.*, **124**, 1767–1785.

624 Damiani, R., G. Vali, and S. Haimov, 2006: The structure of thermals in cumulus from
625 airborne dual-doppler radar observations. *J. Atmos. Sci.*, **63**, 1432–1450, [https://doi.org/](https://doi.org/10.1175/JAS3701.1)
626 10.1175/JAS3701.1.

627 Davis, C. A., K. W. Manning, R. E. Carbone, S. B. Trier, and J. D. Tuttle, 2003: Coherence of
628 warm-season continental rainfall in numerical weather prediction models. *Mon. Wea. Rev.*, **131**,
629 2667–2679.

630 De Rooy, W. C., and Coauthors, 2013: Entrainment and detrainment in cumulus convection: An
631 overview. *Quart. J. Roy. Meteor. Soc.*, **139**, 1–19, <https://doi.org/10.1002/qj.1959>.

632 Demko, J. C., and B. Geerts, 2010: A numerical study of the evolving convective boundary layer
633 and orographic circulation around the Santa Catalina Mountains in Arizona. Part I: Circulation
634 without deep convection. *Mon. Wea. Rev.*, **138**, 1902–1922.

635 Donelan, M. A., B. K. Haus, N. Reul, W. J. Plant, M. Stiassnie, H. C. Graber, O. B. Brown, and
636 E. S. Saltzman, 2004: On the limiting aerodynamic roughness of the ocean in very strong winds.
637 *Geophys. Res. Lett.*, **31**, L18 306.

638 Dörnbrack, A., J. D. Doyle, T. P. Lane, R. D. Sharman, and P. K. Smolarkiewicz, 2005: On physical
639 reliability and uncertainty of numerical solutions. *Atmos. Sci. Lett.*, **6**, 118–122.

640 Duda, J. D., and W. A. Gallus, 2013: The impact of large-scale forcing on skill of simulated
641 convective initiation and upscale evolution with convection-allowing grid spacings in the WRF.
642 *Wea. Forecasting*, **28**, 994–1018, <https://doi.org/10.1175/WAF-D-13-00005.1>.

643 Fairall, C. W., E. F. Bradley, J. E. Hare, A. A. Grachev, and J. B. Edson, 2003: Bulk parameterization
644 of air-sea fluxes: Updates and verification for the COARE algorithm. *J. Climate*, **520**, 571–591.

645 French, J., G. Vali, and R. D. Kelly, 1999: Evolution of small cumulus clouds in Florida: Obser-
646 vations of pulsating growth. *Atmos. Res.*, **52**, 143–165.

647 Grell, G. A., J. Dudhia, and D. R. Stauffer, 1994: A description of the fifth-generation
648 Penn State/NCAR Mesoscale Model (MM5). *NCAR Tech. Note NCAR/TN-398/STR*, 121 pp.,
649 <https://doi.org/10.5065/D62V2D1B>.

650 Hagen, M., J. v. Baelen, and E. Richard, 2011: Influence of the wind profile on the initiation of
651 convection in mountainous terrain. *Quart. J. Roy. Meteor. Soc.*, **137**, 224–235, [https://doi.org/](https://doi.org/10.1002/qj.784)
652 10.1002/qj.784.

653 Hernandez-Deckers, D., and S. C. Sherwood, 2016: A numerical investigation of cumulus thermals.
654 *J. Atmos. Sci.*, **73**, 4117–4136.

655 Hernandez-Deckers, D., and S. C. Sherwood, 2018: On the role of entrainment in the fate of
656 cumulus thermals. *J. Atmos. Sci.*, **75**, 3911–3924.

657 Houston, A. L., and D. Niyogi, 2007: The sensitivity of convective initiation to the lapse rate
658 of the active cloud-bearing layer. *Mon. Wea. Rev.*, **135**, 3013–3032, [https://doi.org/10.1175/](https://doi.org/10.1175/MWR3449.1)
659 MWR3449.1.

660 Iacono, M. J., J. S. Delamere, E. J. Mlawer, M. W. Shephard, S. A. Clough, and W. D. Collins,
661 2008: Radiative forcing by long-lived greenhouse gases: Calculations with the AER radiative
662 transfer models. *J. Geophys. Res.*, **113**, D13 103, <https://doi.org/10.1029/2008jd009944>.

663 Kirshbaum, D. J., 2011: Cloud-resolving simulations of deep convection over a heated mountain.
664 *J. Atmos. Sci.*, **68**, 361–378, <https://doi.org/10.1175/2010JAS3642.1>.

665 Kirshbaum, D. J., 2013: On thermally forced circulations over heated terrain. *J. Atmos. Sci.*, **70**,
666 1690–1709.

667 Kirshbaum, D. J., 2017: On upstream blocking over heated mountain ridges. *Quart. J. Roy. Meteor.*
668 *Soc.*, **143**, 53–68.

669 Kirshbaum, D. J., 2020: Numerical simulations of orographic convection across multiple gray
670 zones. *J. Atmos. Sci.*, **77**, 3301–3320, <https://doi.org/10.1175/JAS-D-20-0035.1>.

671 Kirshbaum, D. J., B. Adler, N. Kalthoff, C. Barthlott, and S. Serafin, 2018: Moist orographic
672 convection: Physical mechanisms and links to surface-exchange processes. *Atmosphere*, **9**, 80,
673 <https://doi.org/10.3390/atmos9030080>.

674 Kirshbaum, D. J., and D. R. Durran, 2004: Factors governing cellular convection in orographic
675 precipitation. *J. Atmos. Sci.*, **61**, 682–698.

- 676 Kirshbaum, D. J., and C. C. Wang, 2014: Boundary layer updrafts driven by airflow over heated
677 terrain. *J. Atmos. Sci.*, **71**, 1425–1442, <https://doi.org/10.1175/JAS-D-13-0287.1>.
- 678 Lecoanet, D., and N. Jeevanjee, 2019: Entrainment in resolved, dry thermals. *J. Atmos. Sci.*, **76**,
679 3785–3801, <https://doi.org/10.1175/JAS-D-18-0320.1>.
- 680 Leger, J., J. P. Lafore, J. M. Piriou, and J. F. Guérémy, 2019: A simple model of convective drafts
681 accounting for the perturbation pressure term. *J. Atmos. Sci.*, **76**, 3129–3149.
- 682 Markowski, P., and Y. Richardson, 2010: *Mesoscale meteorology in Midlatitudes*. Wiley-Blackwell,
683 407 pp.
- 684 Markowski, P. M., C. Hannon, and E. Rasmussen, 2006: Observations of convection initiation “fail-
685 ure” from the 12 June 2002 IHOP deployment. *Mon. Wea. Rev.*, **134**, 375–405, [https://doi.org/](https://doi.org/10.1175/MWR3059.1)
686 [10.1175/MWR3059.1](https://doi.org/10.1175/MWR3059.1).
- 687 Marquis, J. N., A. C. Varble, P. Robinson, T. C. Nelson, and K. Friedrich, 2021: Low-level
688 mesoscale and cloud-scale interactions promoting deep convection initiation. *Mon. Wea. Rev.*,
689 **149**, 2473–2495, <https://doi.org/10.1175/MWR-D-20-0391.1>.
- 690 McKim, B., N. Jeevanjee, and D. Lecoanet, 2020: Buoyancy-driven entrainment in dry thermals.
691 *Quart. J. Roy. Meteor. Soc.*, **146**, 415–425, <https://doi.org/10.1002/qj.3683>.
- 692 Morrison, H., 2016: Impacts of updraft size and dimensionality on the perturbation pressure
693 and vertical velocity in cumulus convection. Part II: Comparison of theoretical and numerical
694 solutions and fully dynamical simulations. *J. Atmos. Sci.*, **73**, 1455–1480, [https://doi.org/10.](https://doi.org/10.1175/JAS-D-15-0041.1)
695 [1175/JAS-D-15-0041.1](https://doi.org/10.1175/JAS-D-15-0041.1).
- 696 Morrison, H., 2017: An analytic description of the structure and evolution of growing deep cumulus
697 updrafts. *J. Atmos. Sci.*, **74** (3), 809–834, <https://doi.org/10.1175/JAS-D-16-0234.1>.
- 698 Morrison, H., J. A. Curry, and V. I. Khvorostyanov, 2005: A new double-moment microphysics
699 parameterization for application in cloud and climate models. Part I: Description. *J. Atmos. Sci.*,
700 **62**, 1665–1677, <https://doi.org/10.1175/JAS3446.1>.

701 Morrison, H., J. M. Peters, W. M. Hannah, A. C. Varble, and S. E. Giangrande, 2020: Thermal
 702 chains in ascending moist updrafts: Part 1: Theoretical description. *J. Atmos. Sci.*, **77**, 3637–
 703 3660, <https://doi.org/10.1175/JAS-D-19-0243.1>.

704 Morrison, H., J. M. Peters, and S. C. Sherwood, 2021: Comparing growth rates of sim-
 705 ulated moist and dry convective thermals. *J. Atmos. Sci.*, **78**, 797–816, [https://doi.org/](https://doi.org/10.1175/JAS-D-10-0166.1)
 706 [10.1175/JAS-D-10-0166.1](https://doi.org/10.1175/JAS-D-10-0166.1).

707 Moser, D. H., and S. Lasher-Trapp, 2017: The influence of successive thermals on entrainment
 708 and dilution in a simulated cumulus congestus. *J. Atmos. Sci.*, **74**, 375–392, [https://doi.org/](https://doi.org/10.1175/JAS-D-16-0144.1)
 709 [10.1175/JAS-D-16-0144.1](https://doi.org/10.1175/JAS-D-16-0144.1).

710 Mulholland, J. P., S. W. Nesbitt, R. J. Trapp, and J. M. Peters, 2020: The influence of terrain on
 711 the convective environment and associated convective morphology from an idealized modeling
 712 prospective. *J. Atmos. Sci.*, **77**, 3929–3949, <https://doi.org/10.1175/JAS-D-19-0190.1>.

713 Nelson, T. C., J. Marquis, A. Varble, and K. Friedrich, 2021: Radiosonde observations of environ-
 714 ments supporting deep moist convection initiation during RELAMPAGO-CACTI. *Mon. Wea.*
 715 *Rev.*, **149**, 289–309, <https://doi.org/10.1175/MWR-D-20-0148.1>.

716 Nesbitt, S. W., and Coauthors, 2021: A storm safari in subtropical South America: proyecto RE-
 717 LAMPAGO. *Bull. Amer. Meteor. Soc.*, **EOR**, 1–64, [https://doi.org/10.1175/BAMS-D-20-0029.](https://doi.org/10.1175/BAMS-D-20-0029.1)
 718 [1](https://doi.org/10.1175/BAMS-D-20-0029.1).

719 Nowotarski, C. J., P. M. Markowski, Y. P. Richardson, and G. H. Bryan, 2014: Properties of a
 720 simulated convective boundary layer in an idealized supercell thunderstorm environment. *Mon.*
 721 *Wea. Rev.*, **142**, 3955–3976.

722 Peters, J. M., W. Hannah, and H. Morrison, 2019: The Influence of Vertical Wind Shear on Moist
 723 Thermals. *J. Atmos. Sci.*, **76** (6), 1645–1659, <https://doi.org/10.1175/JAS-D-18-0296.1>.

724 Peters, J. M., H. Morrison, W. M. Hannah, A. C. Varble, and S. E. Giangrande, 2020: Ther-
 725 mal chains in ascending moist updrafts: Part 2: Simulations. *J. Atmos. Sci.*, **77**, 3661–3681,
 726 <https://doi.org/10.1175/JAS-D-19-0244.1>.

727 Peters, J. M., H. Morrison, T. C. Nelson, J. N. Marquis, J. Mulholland, and C. J. Nowotarski,
728 2021a: The influence of shear on deep convection initiation. Part 1: Theory. *J. Atmos. Sci.*, in
729 review.

730 Peters, J. M., H. Morrison, T. C. Nelson, J. N. Marquis, J. Mulholland, and C. J. Nowotarski,
731 2021b: The influence of shear on deep convection initiation. Part 2: Simulations. *J. Atmos. Sci.*,
732 in review.

733 Romps, D. M., 2010: A direct measure of entrainment. *J. Atmos. Sci.*, **67**, 1908–1927.

734 Rousseau-Rizzi, R., D. J. Kirshbaum, and M. K. Yau, 2017: Initiation of deep convection over
735 an idealized mesoscale convergence line. *J. Atmos. Sci.*, **74**, 835–853, [https://doi.org/10.1175/
736 JAS-D-16-0221.1](https://doi.org/10.1175/JAS-D-16-0221.1).

737 Schumacher, R. S., and Coauthors, 2021: Convective-storm environments in subtropical South
738 America from high-frequency soundings during RELAMPAGO-CACTI. *Mon. Wea. Rev.*, **149**,
739 1439–1458, <https://doi.org/10.1175/MWR-D-20-0293.1>.

740 Sherwood, S. C., D. Hernandez-Deckers, M. Colin, and F. Robinson, 2013: Slippery thermals
741 and the cumulus entrainment paradox. *J. Atmos. Sci.*, **70**, 2426–2442, [https://doi.org/10.1175/
742 JAS-D-12-0220.1](https://doi.org/10.1175/JAS-D-12-0220.1).

743 Singh, I., S. W. Nesbitt, and C. A. Davis, 2021: Quasi-idealized numerical simulations of processes
744 involved in orogenic convection initiation over the Sierras de Córdoba mountains. *J. Atmos. Sci.*,
745 in review.

746 Soderholm, B., B. Ronalds, and D. J. Kirshbaum, 2014: The evolution of convective storms
747 initiated by an isolated mountain ridge. *Mon. Wea. Rev.*, **142**, 1430–1451, [https://doi.org/10.
748 1175/MWR-D-13-00280.1](https://doi.org/10.1175/MWR-D-13-00280.1).

749 Tarshish, N., N. Jeevanjee, and D. Lecoanet, 2018: Buoyant motion of a turbulent thermal. *J.*
750 *Atmos. Sci.*, **75**, 3233–3244, <https://doi.org/10.1175/JAS-D-17-0371.1>.

751 Trier, S., F. Chen, and K. Manning, 2004: A study of convection initiation in a mesoscale model
752 using high-resolution land surface initial conditions. *Mon. Wea. Rev.*, **132**, 2954–2976.

- 753 Trier, S., J. H. Marsham, C. A. Davis, and D. A. Ahijevych, 2011: Numerical simulations of the
754 postsunrise reorganization of a nocturnal mesoscale convective system during 13 June IHOP
755 2002. *J. Atmos. Sci.*, **68**, 2988–3011.
- 756 Varble, A., and Coauthors, 2014: Evaluation of cloud-resolving and limited area model intercom-
757 parison simulations using TWP-ICE observations: 1. Deep convective updraft properties. *J.*
758 *Geophys. Res. Atmos.*, **119**, 13 891–13 918, <https://doi.org/10.1002/2013JD021371>.
- 759 Varble, A. C., and Coauthors, 2021: Utilizing a storm-generating hotspot to study convective
760 cloud transitions: The CACTI experiment. *Bull. Amer. Meteor. Soc.*, **EOR**, 1–67, [https://doi.org/](https://doi.org/10.1175/BAMS-D-20-0030.1)
761 [10.1175/BAMS-D-20-0030.1](https://doi.org/10.1175/BAMS-D-20-0030.1).
- 762 Wang, Q., M. Xue, and Z. Tan, 2016: Convective initiation by topographically induced conver-
763 gence forcing over the Dabie Mountains on 24 June 2010. *Adv. Atmos. Sci.*, **33**, 1120–1136,
764 <https://doi.org/10.1007/s00376-016-6024-z>.
- 765 Wang, S., J. C. Golaz, and Q. Wang, 2008: Effect of intense wind shear across the inversion on
766 stratocumulus clouds. *Geophys. Res. Lett.*, **35**, L15 814, <https://doi.org/10.1029/2008GL033865>.
- 767 Wang, S., X. Zheng, and Q. Jiang, 2012: Strongly sheared stratocumulus convection: an observa-
768 tionally based large-eddy simulation study. *Atmos. Chem. Phys.*, **12**, 5223–5235, [https://doi.org/](https://doi.org/10.5194/acp-12-5223-2012)
769 [10.5194/acp-12-5223-2012](https://doi.org/10.5194/acp-12-5223-2012).
- 770 Weisman, M. L., C. Davis, W. Wang, K. W. Manning, and J. B. Klemp, 2008: Experiences with
771 0–36-h explicit convective forecasts with the WRF-ARW model. *Wea. Forecasting*, **23**, 407–437,
772 <https://doi.org/10.1175/2007WAF2007005.1>.
- 773 Wilson, J. W., and R. D. Roberts, 2006: Summary of convective storm initiation and evolution dur-
774 ing IHOP: Observational and modeling perspective. *Mon. Wea. Rev.*, **134**, 23–47, [https://doi.org/](https://doi.org/10.1175/MWR3069.1)
775 [10.1175/MWR3069.1](https://doi.org/10.1175/MWR3069.1).
- 776 Xue, M., and W. J. Martin, 2006: A high-resolution modeling study of the 24 May 2002 dryline
777 case during IHOP. Part II: Horizontal convective rolls and convective initiation. *Mon. Wea. Rev.*,
778 **134**, 172–191.
- 779 Zhao, M., and P. H. Austin, 2005: Life cycle of numerically simulated shallow cumulus clouds.
780 Part II: Mixing dynamics. *J. Atmos. Sci.*, **62**, 1291–1310, <https://doi.org/10.1175/JAS3415.1>.